Matter and Radiation at Extremes | RESEARCH ARTICLE | scitation.org/journal/mre

Transition of the generation mechanism of high-order harmonics in an extended neon system

Cite as: Matter Radiat. Extremes 7, 044403 (2022); doi: 10.1063/5.0085861
Submitted: 19 January 2022 • Accepted: 16 June 2022 •
Published Online: 12 July 2022

Jingli Gao,[1] Difa Ye,[2] Jie Liu,[1,3] and Wei Kang[1,a)]

AFFILIATIONS

[1] HEDPS, Center for Applied Physics and Technology and College of Engineering, Peking University, Beijing 100871, China
[2] Institute of Applied Physics and Computational Mathematics, Beijing 100088, China
[3] Graduate School, China Academy of Engineering Physics, Beijing 100193, China

[a)] **Author to whom correspondence should be addressed:** weikang@pku.edu.cn

ABSTRACT

Using a time-dependent density functional theory method, we perform a systematic numerical study of the transition of high-order harmonic generation in neon (Ne) systems from an isolated Ne atom to an extended Ne system of solid density. We show that ionized electrons wander in such extended systems until they meet a nearby ion and collide with it. The maximum energy edge for the main feature of the high-order harmonic spectrum in this "wandering electron" picture is determined as $E_{edge} = I_p + 8U_p$, where I_p is the ionization energy of Ne and U_p is the ponderomotive energy delivered by the driving laser. The factor of 8 comes from the maximum kinetic energy of an ionized electron in the driving laser field. Beyond the atomic limit of high-order harmonic spectra, a multiplatform feature is observed, corresponding to re-collisions of ionized electrons with their nearby ions. It is also shown that a Ne simple cubic lattice of appropriate size provides a selection condition for the direction of polarization of high-order harmonics beyond the atomic limit, which may be further used to manipulate the emitted radiation.

I. INTRODUCTION

High-order harmonic generation (HHG) is generally believed to be the fundamental process underlying a broad range of attosecond applications, such as attosecond control and measurements,[1–8] and is therefore one of the main focuses of current attosecond science. Increasing the brightness and cutoff energy,[9–12] i.e., the maximum photon energy, of high-order harmonics has been of central importance for applications of HHG ever since its first demonstration in gases,[2] since this enables higher resolution in photography of ultrafast electrons,[13] higher accuracy in tracking the evolution of chemical reactions,[14] and higher precision in steering electron wave packets in molecules.[9,10,15]

At present there are two parallel approaches to the generation of high-order harmonics, based on different theoretical principles. HHG in gases is widely used to produce coherent extreme-ultraviolet attosecond pulses.[2,5,16] The mechanism involved here can be described in terms of a semiclassical "three-step" process[16–19] in which high-order harmonic radiation is generated when an electron, ionized from its ground state, re-collides with its parent ion after it has oscillated for half a cycle in the intense driving laser field. The scenario for HHG in solids is quite different, involving several competing mechanisms, each of which provides a channel for HHG.[20–25] In addition to interband transitions, which are reminiscent of the atomic semiclassical mechanism, intraband Bloch oscillations of electrons and holes derived from lattice structure are also important sources of high-order harmonics in solids.[26–28] For the most recent progress in this direction, the reader should consult Ref. 29 and the description therein of the Wannier quasiclassical model, which illustrates the importance of intersite interaction. Emitted high-order harmonic radiation is the result of interfering superposition of all these channels.

From the perspective of applications of HHG, the "three-step" mechanism in gases might be considered preferable, since it provides

a single channel of HHG and therefore much easier to control.[17,19] However, as far as the intensity of emitted radiation is concerned, the high density of atoms in solids and their regular lattice configuration are of particular significance.[20,30,31] It has been demonstrated experimentally by Popmintchev *et al.*[11] that a fine balance between a high intensity of emitted radiation and the atomic mechanism of HHG can be attained in gases at high pressure (up to 30 atm for noble gases), corresponding to an average distance d_0 between two atoms of about 11 Å. At this distance, there is negligible overlap of the ground-state wave functions of different atoms, which effectively suppresses the HHG channel associated with the hole dynamics typical of solids. However, experiments have also revealed that a new channel of HHG emerges, associated with re-collisions of electrons with nearby ions.

How the HHG mechanism is transformed from the atomic "three-step" one[17,19] to the multichannel one[32–34] in solids is therefore an important question, the answer to which may help provide not only further insights into HHG itself, but also detailed theoretical guidance for the design of HHG devices. In addition to various simplified theoretical models of the transition of the HHG mechanism,[18,33,35–38] there are also some first-principles approaches that have been applied successfully to this problem. One of these is the time-dependent density functional theory (TDDFT) method,[39–41] which affords a quantum-mechanical description of the time evolution of electrons in the system based on the time-dependent Kohn–Sham equations. Previous work on semiconductors and insulators has shown that the TDDFT method performs satisfactorily in its predictions of HHG in various solids.[32,42–47] However, it is not trivial to apply the same approach to the description of HHG in a system of gaseous density, because of the tremendous computational cost then incurred, since this cost scales roughly as d_0^3, with d_0 being the distance between atoms. However, with the most recent advances in computational techniques and a much improved implementation of the TDDFT method,[48–51] it is now possible to get reliable predictions for low-density systems such as noble gases at 0.06 atm, corresponding to $d_0 \approx 85$ Å (160 bohrs). This paves the way for the creation of a physical picture of the transition of the HHG mechanism.

In this work, with the TDDFT method[39–41] as our tool, we present a systematic numerical study of the transition of HHG in neon (Ne) systems. The density of the system varies from that of an isolated Ne atom to that of solid Ne, namely, 3.55×10^{22} cm^{-3}, corresponding to an average distance $d_0 = 3.04$ Å (5.75 bohrs). We show that in an extended system, ionized electrons wander about in the system until they meet a nearby ion and collide with it. There is no maximum distance limit as in the atomic HHG mechanism, and the maximum kinetic energy of the recombined electron is then determined to be $3.2U_p$,[17,52] with $U_p = I_0/(4\omega^2)$ being the ponderomotive energy delivered by a laser of frequency ω and intensity I_0. Note that throughout this article, the formulas are all expressed in atomic units. The edge of the main feature of the high-order harmonic spectrum in this "wandering electron" picture is then given by $E_{\text{edge}} = I_p + 8U_p$, where I_p is the ionization energy of Ne. The factor of 8 comes from the maximum kinetic energy of an ionized electron in the driving laser field. Beyond the atomic limit of high-order harmonic spectra, a multiplatform feature is observed, corresponding to re-collisions of ionized electrons with nearby ions. In addition, it is shown that a Ne simple cubic lattice of size 63.5 Å (120 bohrs) provides a selection condition for the direction of polarization of high-order harmonics beyond the atomic limit, which may be further used to manipulate the emitted radiation.

The remainder of this article is organized as follows. After reviewing the theoretical method in Sec. II, we present our main results in Sec. III, where the transition of the HHG mechanism and the energy edge in a low-density gas system are discussed in detail. A short summary is provided in Sec. IV.

II. SIMULATION METHOD

TDDFT describes the evolution of Kohn–Sham orbitals of a multi-electron system using the time-dependent Kohn–Sham equations,

$$i\frac{\partial}{\partial t}\psi_\alpha(\mathbf{r},t) = \left\{-\frac{\nabla^2}{2} + V_{\text{ext}}(\mathbf{r},t) + V_H[n(\mathbf{r},t)] + V_{\text{xc}}[n(\mathbf{r},t)]\right\}\psi_\alpha(\mathbf{r},t), \tag{1}$$

following the arguments of Runge and Gross.[39–41] Here, α is the index of a Kohn–Sham orbital, $\psi_\alpha(\mathbf{r},t)$ is the wave function, V_{ext} is the external potential (including the ionic potential, the trapping potential of the atoms, and the applied laser field), V_H is the Hartree part of the Coulomb interaction between electrons, and V_{xc} is the time-dependent exchange-correlation potential. The electron density is $n(\mathbf{r},t) = \sum_\alpha |\psi_\alpha(\mathbf{r},t)|^2$, and the electronic current density $\mathbf{j}(\mathbf{r},t)$ is calculated as[32,53]

$$\mathbf{j}(\mathbf{r},t) = \frac{i}{2}\sum_\alpha\left[\psi_\alpha^*(\mathbf{r},t)\nabla\psi_\alpha(\mathbf{r},t) - \psi_\alpha(\mathbf{r},t)\nabla\psi_\alpha^*(\mathbf{r},t)\right]. \tag{2}$$

The high-order harmonic spectrum is obtained as the Fourier transform of the rate of change of the laser-driven electronic current:[32]

$$\text{HHG}(\omega) = \left|\text{FT}\left\{\frac{\partial}{\partial t}\int_\Omega d^3\mathbf{r}\,\mathbf{j}(\mathbf{r},t)\right\}\right|^2, \tag{3}$$

where Ω represents the volume of the system and FT denotes the Fourier transform operation. Note that for the calculation of the time-dependent high-order harmonic spectrum, a small Gaussian time window of 0.13 fs width will be used in Eq. (3) before Fourier transformation. When attosecond pulses [e.g., an isolated attosecond pulse (IAP) or a pair of attosecond pulses] can be constructed from high-order harmonic spectra, they are calculated as coherent superpositions of consecutive harmonics in a given frequency window from ω_l to ω_h as follows:[9]

$$I(t) = \left|\sum_{\omega_l}^{\omega_h} e^{i\omega t}\,\text{FT}\left\{\frac{\partial}{\partial t}\int_\Omega d^3\mathbf{r}\,\mathbf{j}(\mathbf{r},t')\right\}\right|^2. \tag{4}$$

In our calculations, Ne atoms are placed at lattice points of a three-dimensional simple cubic optical lattice for simplicity of calculation. The optical lattice can be generated by the potential of three pairs of identical laser beams,[54] as illustrated schematically in Fig. 1(a), which form standing waves in three orthogonal directions. The resulting optical potential can be written as

$$V(x,y,z) = V_0[\sin^2(k_L x) + \sin^2(k_L y) + \sin^2(k_L z)], \tag{5}$$

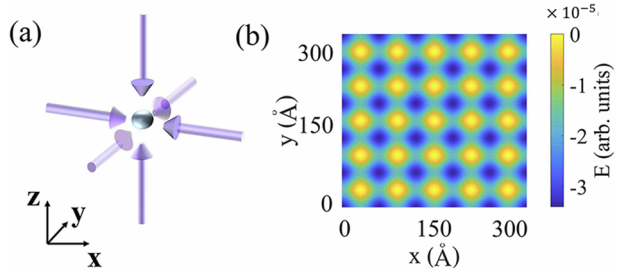

FIG. 1. (a) Schematic illustration of the laser configuration to form a simple cubic optical lattice. (b) Top view (x–y plane) of the simple cubic lattice.

which provides the symmetry of a simple cubic lattice. A top view of the potential is shown in Fig. 1(b). Here k_L is the wave vector of the periodic potential, determined by the wavelength λ_L of the laser beam as $k_L = 2\pi/\lambda_L$. The lattice constant is given by $d = \lambda_L/2$. V_0 is the potential depth of the standing waves, sometimes expressed using the recoil energy $E_r = k_L^2/(2m)$ as the unit, with m being the mass of the Ne atom, as a direct measure of its ability to confine atoms. In our calculations, E_r is of the order of 10^{-4} eV, and V_0 is set to be about $100E_r$ and thus has negligible influence on the energetic behavior of electrons. It should be noted that with current techniques, it is only possible to generate optical lattices with lattice constants of several hundreds of nanometers or longer. Optical lattices with a shorter lattice constant are still theoretical constructs. However, they will be considered as a convenient theoretical tool in this work, mainly to take account of density effects.

All calculations are performed using the OCTOPUS code,[48–51] which is a real-space implementation of the TDDFT method. A primitive unit cell with periodic boundary conditions is used, except for the case of an isolated Ne atom, where a spherical calculation region of 100 bohrs (52.9 Å) radius is used with absorbing boundary conditions. The width of the absorbing region is 25 bohrs (13.2 Å), inside which there is a sine-square-shaped imaginary absorbing potential with a scaling factor −2.0 hartree (−54.4 eV), following De Giovannini *et al.*[55] The resolution of the real space is 0.4 bohr (0.21 Å), and the energy cutoff of the kinetic energy is set to be 30.84 hartree (839.2 eV). The k-point mesh used to sample the Brillouin zone[56] varies from $2 \times 2 \times 2$ for $d = 160$ bohrs (84.7 Å) to $24 \times 24 \times 24$ for $d = 5.75$ bohrs (3 Å), increasing with decreasing lattice constant. The time step to advance the evolution of the electronic wave functions is 0.48 as, and the exchange-correlation interaction is described by the adiabatic local density approximation (ALDA), with the parameterization of Perdew and Zunger.[57] The Ne pseudopotential has a norm-conserving Troullier–Martins[58] form with eight electrons included explicitly and a cutoff radius of 2.6 bohrs (1.38 Å). Before the system is put into time-dependent evolution, the initial structure and ground-state electronic structure are first generated from a time-independent density functional theory (DFT) calculation.[59,60]

The driving laser pulse is described by a vector potential

$$\mathbf{A}(t) = \frac{\sqrt{8\pi I_0/c}}{\omega} S(t)\cos(\omega t + \phi_0)\hat{\mathbf{e}}, \tag{6}$$

where I_0 is the peak intensity, c is the speed of light, ω is the fundamental frequency of the driving laser, $S(t)$ is the envelope function,

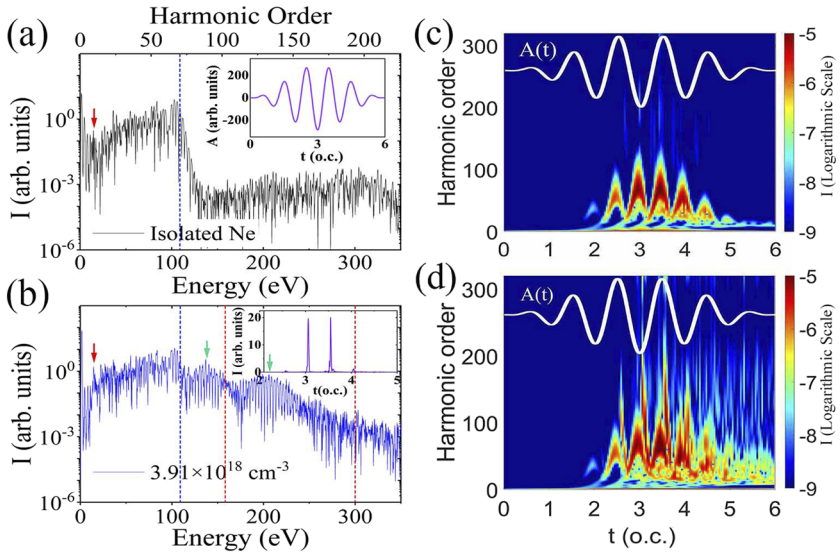

FIG. 2. (a) High-order harmonic spectrum of an isolated Ne atom, with the shape of the driving pulse displayed in the inset. (b) High-order harmonic spectrum of Ne in a simple cubic extended system with a number density 3.91×10^{18} cm^{-3}, corresponding to a lattice constant $d = 120$ bohrs (63.5 Å). The pulse polarization is along the [100] direction. The vertical blue dashed line in (a) and (b) indicates the cutoff energy of high-order harmonics in an isolated Ne atom. The inset in (b) shows the generation of a pair of attosecond pulses, and the energy window is between 158.2 and 300 eV, shown by the vertical red dashed lines. The red arrow shows the bandgap energy of the extended system. The green arrows indicate the peak positions of the two platforms beyond the atomic limit. (c) and (d) Time–frequency analyses of the high-order harmonics in (a) and (b), respectively, where the unit of time is one oscillating cycle (o.c.) of the driving laser pulse, displayed at the top of (c) and (d).

$\hat{\mathbf{e}}$ is the polarization vector, and ϕ_0 is the carrier envelope phase. In the calculations, the fundamental wavelength of the driving laser is 8000 Å, corresponding to $\omega = 1.55$ eV, and the peak intensity is between 50 and 700 TW/cm^2. In the calculation of high-order harmonic spectra, the pulse has a duration $T = 16$ fs, corresponding to six oscillating cycles, and a sine-square envelope $S(t) = \sin^2(\pi t/T)$, as displayed in Fig. 2(a). In the calculation of the IAP, the envelope is set as $S(t) = \sin^{3.7}(\pi t/T)$, with a pulse duration of 13.33 fs, i.e., five oscillating cycles. The carrier envelope phase ϕ_0 is set to be $3\pi/2$ for the generation of the IAP; otherwise, it is set to be zero. Since the wavelength of the driving laser is much longer than the lattice constant d, which varies from 5.75 bohrs (3 Å) to 160 bohrs (84.7 Å), the field felt by the electron in the primitive cell is approximated as a time-dependent uniform field.

III. RESULTS AND DISCUSSION

A. HHG of Ne in a low-density extended system

We first show the general features of HHG in a Ne system at a density comparable to gaseous density. For simplicity of calculation, the Ne atom is assumed to be placed in a simple cubic optical lattice. In Fig. 2(b), a typical high-order harmonic spectrum of Ne is displayed (on a logarithmic scale), where the intensity of the laser is 500 TW/cm^2, the driving field is along the [100] direction of the simple cubic lattice, and the lattice constant $d = 120$ bohrs (63.5 Å), corresponding to a number density of 3.91×10^{18} cm^{-3}. The pulse duration is 16 fs, consisting of six oscillating cycles of the driving laser, as displayed in the inset of Fig. 2(a). A time-dependent high-order harmonic spectrum, calculated as the Fourier transform in a small time window of 0.13 fs, is also displayed in Fig. 2(d) to show the timing of HHG.

For comparison, the high-order harmonic spectrum of an isolated Ne atom is also displayed in Fig. 2(a). The atomic energy cutoff of high-order harmonics given by Refs. 17 and 52 $E_{\text{cut}} = I_p + 3.2U_p$ is shown by the vertical blue dashed line. It can be seen from Fig. 2(a) that at E_{cut}, which is about 110 eV or the 70th order of harmonics for an Ne atom, the spectrum displays a sharp edge, beyond which the intensity decreases to about 10^{-4} of its maximum value. The time-dependent high-order harmonic spectrum in Fig. 2(c) shows that higher-order harmonics are generated in every half cycle of the driving laser field. Both features agree well with the prediction of the semiclassical "three-step" model, showing that the TDDFT calculation indeed captures the main features of HHG of isolated atoms.

By contrast, the high-order harmonic spectrum of an extended system has a typical multiplatform structure, as displayed in Fig. 2(b). Below the atomic energy cutoff, the spectrum is very similar to that of an isolated atom, showing the persistence of the semiclassical mechanism of HHG, i.e., the recombination of ionized electrons with their parent ions. Beyond the energy limit, two extra platforms are observed, corresponding to the re-collision of electrons with their nearest-neighbor and next-nearest-neighbor ions. The platform region ends up at a new energy limit of about 250 eV, corresponding to the 160th order of harmonics. As we shall show in the following discussion, this energy limit is determined by the maximum energy delivered by the driving laser to an ionized electron.

For isolated atoms, the energy cutoff E_{cut} of the high-order harmonic spectrum is mainly determined by the maximum distance that an electron can reach before re-collision with its parent ion.[17,52] In an extended system, however, one can expect that this distance limit will no longer apply. Instead, in a semiclassical picture, an ionized electron can wander around the extended system until it meets an ion and recombines with it. Although the position of the electron is not known exactly during its wandering, its maximum kinetic energy is determined by the acceleration and deceleration process of the driving field and turns out to be $8U_p$ at the moment when the electron is accelerated for a half cycle. Thus, the maximum energy of the high-order harmonic spectrum is given by the maximum kinetic energy plus the ionization energy, i.e., $E_{\text{cut}}^{\text{new}} = I_p + 8U_p$.

The wandering electron picture suggests that the HHG process is no longer synchronized with the driving cycles, and this is indeed observed in the time-dependent high-order harmonic spectrum displayed in Fig. 2(d). Compared with the time-dependent high-order harmonic spectrum of an isolated Ne atom in Fig. 2(c), it can be seen that the high-order harmonics can still be generated in the fifth cycle. Since the laser field in the fifth cycle is not strong enough to ionize additional electrons, as illustrated in the case of the isolated Ne atom, these high harmonics are actually generated by wandering electrons ionized in previous driving cycles.

To confirm that the platforms beyond the atomic energy cutoff in Fig. 2(b) originate from the collision of an electron with its nearby ions, energy distributions of an electron at the times at which it arrives at the nearest-neighbor ion and the next-nearest-neighbor ion are plotted in Fig. 3. The results are calculated using the semiclassical model, which assumes that an electron is accelerated only by the driving field without an initial velocity after it was ionized at a certain moment in the driving cycle. The ionization probability is assumed to be proportional to the intensity of the driving field, which is set to be monochromatic with an intensity of 500 TW/cm^2 at $\lambda_L = 8000$ Å. The lattice constant used in the calculation is $d = 120$ bohrs (63.5 Å). Figure 3 shows that the energy distribution of an electron arriving at the nearest-neighbor ion (dark cyan curve) has a peak at around 130 eV, and goes down to zero at the

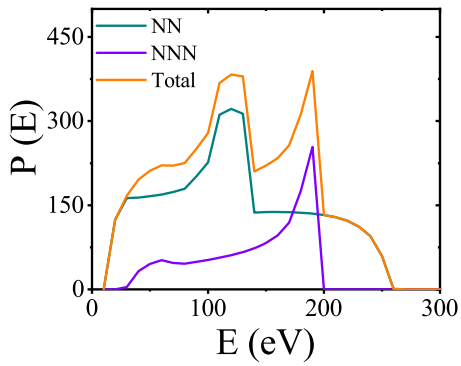

FIG. 3. Energy distribution of an ionized electron at the moment when it arrives at the nearest-neighbor (NN) ion, shown as the green curve, and the next-nearest-neighbor (NNN) ion, shown as the purple curve. The total distribution is shown as the orange curve. The distribution is calculated using a semiclassical model with $d = 120$ bohrs (63.5 Å). The driving laser is assumed to be monochromatic with an intensity of 500 TW/cm^2 at $\lambda_L = 8000$ Å.

maximum energy 250 eV. The energy distribution of an electron at the next-nearest-neighbor ion (violet curve) has a peak at a higher energy around 200 eV. The total distribution (orange curve) agrees qualitatively with the TDDFT result displayed in Fig. 2(b).

B. Transition of HHG mechanism

To understand how the transition in the HHG mechanism occurs with increasing ionic density, a series of calculations are carried out at different ionic densities ranging from nearly zero, i.e., the isolated atom case, to the density of solid Ne, where d is about 5.75 bohrs (3 Å). Figure 4 shows the calculated high-order harmonic spectra for several ionic densities. The density of the system decreases from Figs. 4(a)–4(d). It can be seen that below a density of 1.65×10^{18} cm^{-3}, where d = 160 bohrs (84.7 Å), the high-order harmonic spectra are atomic-like. The wandering of electrons is not significant. At higher densities, the high-order harmonic spectra show typical multiplatform features beyond the atomic energy cutoff. All of these features disappear at the maximum energy around $8U_p + I_p$. It is interesting to notice that, in this density regime, the number of platforms increases with increasing density, showing that the electrons can recombine with ions that are not close to their parent ions, which provides further support for the picture of wandering electrons. When the ionic density reaches 3.55×10^{22} cm^{-3}, i.e., the density of solid Ne, the high-order harmonic spectrum still displays some of the features of wandering electrons. In particular, the maximum energy limit of $8U_p + I_p$ can still be observed, but the multiplatform features are smoothed out.

The transition from an atomic-like spectrum of an isolated atom to the multiplatform spectrum of a low-density extended structure in Fig. 4 is due mainly to the finite duration of the driving laser pulse. Figure 5 shows the energy distributions of an electron ionized at different moments in the first oscillating cycle of the driving laser. The distributions are calculated at the ends of the first, second, and third cycles, respectively, at each of which two peaks are observed, corresponding to the energy distribution of electrons ionized in the first and second half cycles, respectively. The three distributions show that the maximum energy of the electron recorded at the end of an oscillating cycle is less than 70 eV, which is below the atomic energy limit of 110 eV. This suggests that the energy of an electron will not exceed the atomic energy limit given by Refs. 17 and 52 $I_p + 3.2U_p$ if the pulse finishes with a complete driving cycle. Therefore, for a very long distance between two nearby atoms, the ionized electron is not able to reach its nearest-neighbor ions before the end of the pulse duration, and the energy it carries will not exceed the atomic energy limit, as revealed in Fig. 5. At the given laser intensity of I_L = 500 TW/cm^2, the transition takes place at a density of about 1.65×10^{18} cm^{-3}, corresponding to d = 160 bohrs (84.7 Å).

The transition of the high-order harmonic spectrum to one of a solid type at further increased density probably results from the formation of a solid-like band structure,[61] where significant band distortion occurs at the edges of Brillouin zones owing to strong interactions between atoms at short distances. When this condition holds, the HHG mechanism is dominated by a combination of Bloch oscillations and electronic transitions between bands.[34,62] However,

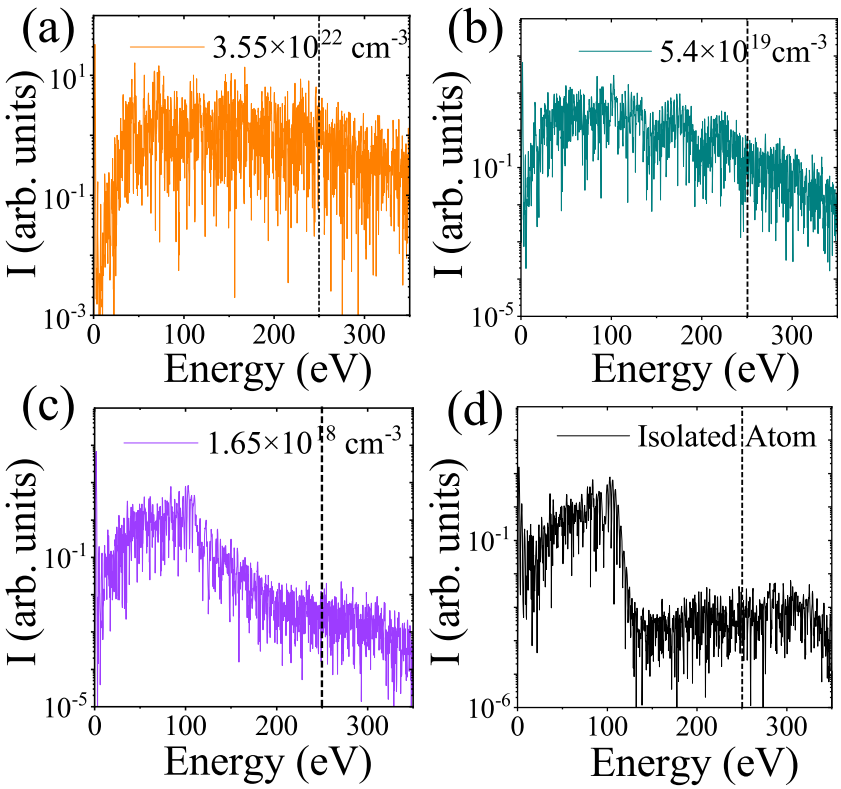

FIG. 4. High-order harmonic spectra for different ionic densities, showing the transition of the HHG mechanism from an isolated Ne (d), to an extended system of solid density (a). The black dashed lines indicate the maximum energy edge of 250 eV. Calculations were performed by the TDDFT method. The laser intensity for the calculations was 500 TW/cm^2 and the wavelength was 8000 Å. The pulse duration was 16 fs.

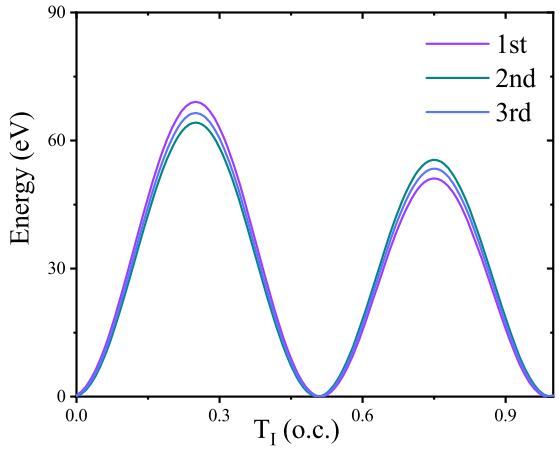

FIG. 5. Energy of a wandering electron at the end of the first, second, and third oscillating cycles of the driving laser, plotted as a function of the time at which it is ionized T_I in the first oscillating cycle of the laser field. The laser configuration is the same as that in Fig. 3.

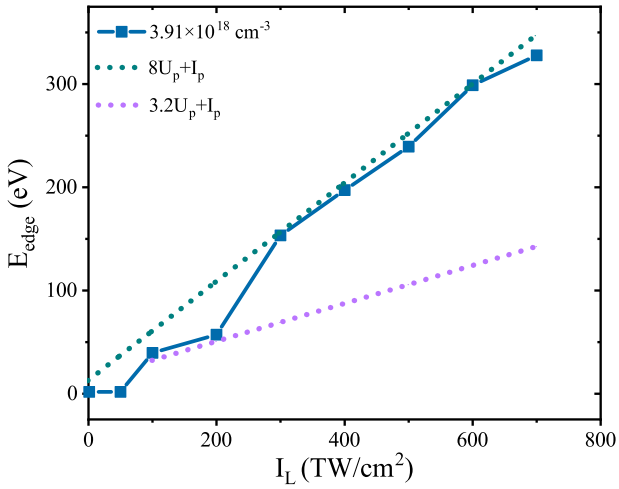

FIG. 7. Laser intensity dependence of the high-order harmonic energy edge calculated at an Ne density of 3.91×10^{18} cm^{-3}, corresponding to $d = 120$ bohrs (63.5 Å). The atomic limit and the new limit of $8U_p + I_p$ are displayed as dotted lines for comparison.

the transition of the band structure is not significant even in the solid Ne case. The band structure of the simple cubic structure at the density of solid Ne is displayed in Fig. 6, where it can be seen that the band structure is quite close to that of a free electron, shown by dotted curves, as a result of weak van der Waals interactions between Ne atoms. Therefore, it is not surprising that the high-order harmonic spectrum at this density still has the same maximum energy limit of about 250 eV.

One can also calculate the dependence of the high-order harmonic energy edge on the intensity of the driving laser. Figure 7 shows the calculated intensity dependence at an ionic density of 3.91×10^{18} cm^{-3}, corresponding to $d = 120$ bohrs (63.5 Å). It can be seen that there is a minimum intensity threshold at around 50 TW/cm^2 for the high-order harmonics being observed. Furthermore, there is a threshold intensity of about 250 TW/cm^2, below which the maximum energy of high-order harmonics satisfies the atomic limit, as a result of finite pulse duration, i.e., the edge of the main feature is $I_p + 3.2U_p$. When the intensity is above the threshold, the energy edge closely follows the straight line corresponding to $8U_p + I_p$.

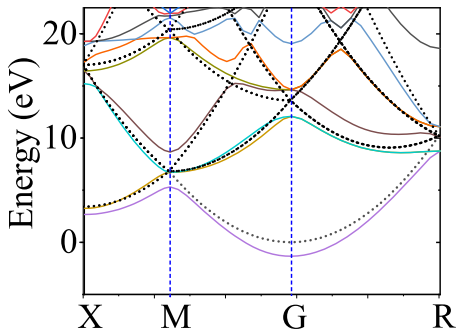

FIG. 6. Band structure (solid curves) of Ne in a simple cubic lattice with a solid density, corresponding to $d = 5.75$ bohrs (3 Å), compared with the band structure of an free electron (dotted curves). The two band structures are similar, as a result of weak van der Waals interaction between Ne atoms.

C. Generation of attosecond pulses and manipulation of the periodic structure

The coherence of the high-order harmonics is retained well in the low-density extended system. A good indication of this is the generation of attosecond pulses. The inset of Fig. 2(b) shows the generation of a pair of attosecond pulses, which are calculated in a simple cubic periodic system with $d = 120$ bohrs, a laser intensity $I_L = 500$ TW/cm^2, and a sine-square-shaped driving laser pulse containing six cycles, as described in Sec. II. The carrier envelope phase ϕ_0 is set to be zero, and the energy window is between 158.2 and 300 eV [the interval between the two vertical red dashed lines in Fig. 2(b)]. From the time-dependent high-order harmonic spectrum in Fig. 2(c), it can be seen that the harmonics in the given energy window start from the third cycle of the pulse and last for about three cycles, which suggests that the attosecond pulses result from coherent superposition of high-order harmonics with interference cancellation. The width of each pulse is about 60 as, and the separation between the two pulses is about half of the cycle, i.e., 1.3 fs. An IAP can also be generated from high-order harmonics with a shorter driving pulse and an appropriately adjusted carrier envelope phase. Figure 8 displays an IAP calculated with a femtosecond driving pulse, for which the envelope function $S(t) = \sin^{3.7}(\pi t/T)$, with $T = 13.33$ fs, i.e., five oscillating cycles. The energy window is between 140 and 300 eV. In this way, it is possible to generate an IAP with a width of about 57 as.

The wandering electron picture and the multiplatform feature of the high-order harmonic spectrum are associated in particular with the effect of the density of the system. However, an extra dimension for the manipulation of HHG may be afforded by the

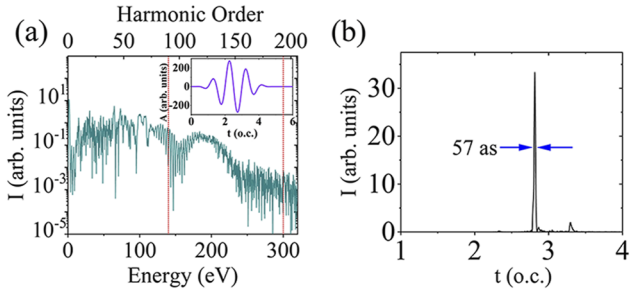

FIG. 8. (a) High-order harmonic spectrum of a $\sin^{3.7}(\omega/T)$-shaped pulse, as displayed in the inset. The carrier envelope phase $\phi_0 = 3\pi/2$, and the duration of the pulse T = 13.33 fs. (b) IAP generated in the energy window from 140 to 300 eV [shown by the vertical dotted lines in (a)]. The laser intensity is 500 TW/cm^2, and the pulse polarization is along the [100] direction. The width of the IAP is about 57 as.

presence of a periodic structure. Figure 9 illustrates how the direction of polarization can be selected in a simple cubic lattice. This selection takes advantage of the fact that the transition from an isolated atomic high-order harmonic spectrum to the multiplatform spectrum occurs at a lattice constant $d \approx 160$ bohrs (84.6 Å) for a laser intensity I_L = 500 TW/cm^2. When the lattice constant d is set to be 120 bohrs (63.5 Å), the lattice can exert a selection effect on the direction of polarization of the driving laser. As can be seen in Fig. 9, only when the polarization is parallel to the [100] direction can the high-order harmonics beyond the atomic energy limit be generated. In the other two diagonal directions, i.e., along [110] and [111], the multiplatform feature is suppressed because of the increased distance between Ne atoms.

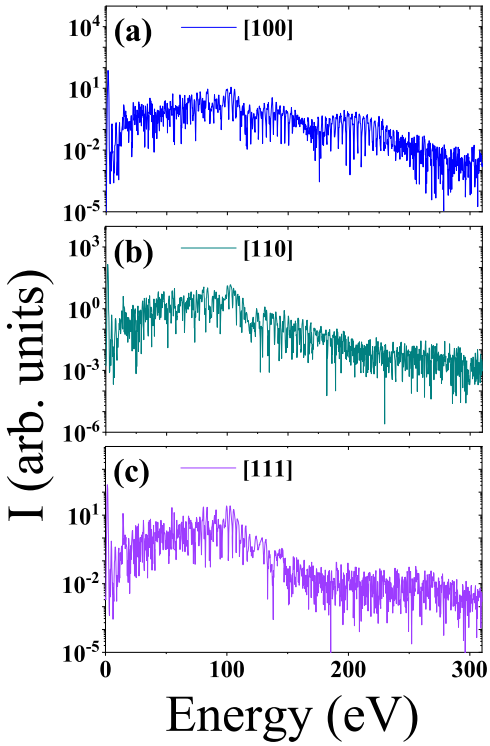

FIG. 9. Selection of direction of polarization in a simple cubic lattice with d = 120 bohrs (63.5 Å). (a)–(c) High-order harmonic spectra generated by a laser with direction of polarization along the [100], [110], and [111] directions, respectively. High-order harmonics beyond the atomic limit can only be observed in the [100] direction.

IV. CONCLUSION

Using real-time time-dependent density functional theory calculations, we have systematically investigated the transition of the HHG mechanism in an isolated Ne atom to that in an extended Ne system of solid density. For the generation of high-order harmonics in such systems, we have presented a wandering electron picture that accounts for the multiplatform feature of high-order harmonic spectra and predicts the energy edge to be $8U_p + I_p$. We have also shown that the high-order harmonics generated in this way may be used to generate an IAP of pulse width about 57 as. In addition, we have found that periodic lattices exhibit an extra selection effect depending on the direction of polarization of the driving laser, which may provide a new way to manipulate high-order harmonics. These interesting observations may help to provide not only a more complete picture of the HHG mechanism, but also new theoretical insights to aid in the design of future HHG devices.

ACKNOWLEDGMENTS

This work is financially supported by the National Key Research and Development Program of China (Grant No. 2017YFA0404200) and the National Natural Science Foundation of China (Grant Nos. 12174034 and 91752202). Some of the calculations were carried out at the National Supercomputer Center in Gangzhou.

AUTHOR DECLARATIONS

Conflict of Interest

The authors have no conflicts to disclose.

Author Contributions

Jingli Gao: Data curation (equal); Investigation (equal); Visualization (equal); Writing – original draft (equal); Writing – review & editing (equal). **Difa Ye:** Conceptualization (equal); Formal analysis (equal); Investigation (equal); Resources (equal); Writing – review & editing (equal). **Jie Liu:** Conceptualization (equal); Formal analysis (equal); Resources (equal); Validation (equal); Writing – review & editing (equal). **Wei Kang:** Conceptualization (equal); Formal analysis (equal); Funding acquisition (equal); Investigation (lead); Methodology (equal); Project administration (equal); Resources (equal); Software (equal); Supervision (equal); Validation (equal); Writing – original draft (equal); Writing – review & editing (equal).

DATA AVAILABILITY

The data that support the plots within this paper and other findings of this study are available from the corresponding authors upon reasonable request.

REFERENCES

[1]F. Krausz and M. Ivanov, "Attosecond physics," Rev. Mod. Phys. **81**, 163–234 (2009).
[2]M. Hentschel, R. Kienberger, C. Spielmann, G. A. Reider, N. Milosevic, T. Brabec, P. Corkum, U. Heinzmann, M. Drescher, and F. Krausz, "Attosecond metrology," Nature **414**, 509–513 (2001).
[3]P. B. Corkum and F. Krausz, "Attosecond science," Nat. Phys. **3**, 381–387 (2007).
[4]A. McPherson, G. Gibson, H. Jara, U. Johann, T. S. Luk, I. A. McIntyre, K. Boyer, and C. K. Rhodes, "Studies of multiphoton production of vacuum-ultraviolet radiation in the rare gases," J. Opt. Soc. Am. B **4**, 595–601 (1987).
[5]P. M. Paul, E. S. Toma, P. Breger, G. Mullot, F. Augeé, P. Balcou, H. G. Muller, and P. Agostini, "Observation of a train of attosecond pulses from high harmonic generation," Science **292**, 1689–1692 (2001).
[6]I. P. Christov, M. M. Murnane, and H. C. Kapteyn, "High-harmonic generation of attosecond pulses in the 'single-cycle' regime," Phys. Rev. Lett. **78**, 1251–1254 (1997).
[7]P. B. Corkum, N. H. Burnett, and M. Y. Ivanov, "Subfemtosecond pulses," Opt. Lett. **19**, 1870–1872 (1994).
[8]R. A. Bartels, A. Paul, H. Green, H. C. Kapteyn, M. M. Murnane, S. Backus, I. P. Christov, Y. Liu, D. Attwood, and C. Jacobsen, "Generation of spatially coherent light at extreme ultraviolet wavelengths," Science **297**, 376–378 (2002).
[9]M. Chini, K. Zhao, and Z. Chang, "The generation, characterization and applications of broadband isolated attosecond pulses," Nat. Photonics **8**, 178–186 (2014).
[10]S. Neppl, R. Ernstorfer, A. L. Cavalieri, C. Lemell, G. Wachter, E. Magerl, E. M. Bothschafter, M. Jobst, M. Hofstetter, U. Kleineberg, J. V. Barth, D. Menzel, J. Burgdörfer, P. Feulner, F. Krausz, and R. Kienberger, "Direct observation of electron propagation and dielectric screening on the atomic length scale," Nature **517**, 342–346 (2015).
[11]T. Popmintchev, M.-C. Chen, D. Popmintchev, P. Arpin, S. Brown, S. Ališauskas, and G. Andriukaitis, "Bright coherent ultrahigh harmonics in the keV X-ray regime from mid-infrared femtosecond lasers," Science **336**, 1287–1291 (2012).
[12]M.-C. Chen, P. Arpin, T. Popmintchev, M. Gerrity, B. Zhang, M. Seaberg, D. Popmintchev, M. M. Murnane, and H. C. Kapteyn, "Bright, coherent, ultrafast soft X-ray harmonics spanning the water window from a tabletop light source," Phys. Rev. Lett. **105**, 173901 (2010).
[13]H. Lakhotia, H. Y. Kim, M. Zhan, S. Hu, S. Meng, and E. Goulielmakis, "Laser picoscopy of valence electrons in solids," Nature **583**, 55–59 (2020).
[14]H. J. Wörner, J. B. Bertrand, D. V. Kartashov, P. B. Corkum, and D. M. Villeneuve, "Following a chemical reaction using high-harmonic interferometry," Nature **466**, 604–607 (2010).
[15]M. Nisoli, P. Decleva, F. Calegari, A. Palacios, and F. Martín, "Attosecond electron dynamics in molecules," Chem. Rev. **117**, 10760–10825 (2017).
[16]E. Constant, D. Garzella, P. Breger, E. Mével, C. Dorrer, C. Le Blanc, F. Salin, and P. Agostini, "Optimizing high harmonic generation in absorbing gases: Model and experiment," Phys. Rev. Lett. **82**, 1668–1671 (1999).
[17]K. J. Schafer, B. Yang, L. F. DiMauro, and K. C. Kulander, "Above threshold ionization beyond the high harmonic cutoff," Phys. Rev. Lett. **70**, 1599–1602 (1993).
[18]M. Lewenstein, P. Balcou, M. Y. Ivanov, A. L'Huillier, and P. B. Corkum, "Theory of high-harmonic generation by low-frequency laser fields," Phys. Rev. A **49**, 2117–2132 (1994).
[19]P. B. Corkum, "Plasma perspective on strong field multiphoton ionization," Phys. Rev. Lett. **71**, 1994–1997 (1993).
[20]S. Ghimire, A. D. DiChiara, E. Sistrunk, P. Agostini, L. F. DiMauro, and D. A. Reis, "Observation of high-order harmonic generation in a bulk crystal," Nat. Phys. **7**, 138–141 (2011).
[21]S. Ghimire and D. A. Reis, "High-harmonic generation from solids," Nat. Phys. **15**, 10–16 (2019).
[22]J. D. Cox, A. Marini, and F. J. G. de Abajo, "Plasmon-assisted high-harmonic generation in graphene," Nat. Commun. **8**, 14380 (2017).
[23]D. Franz, S. Kaassamani, D. Gauthier, R. Nicolas, M. Kholodtsova, L. Douillard, J.-T. Gomes, L. Lavoute, D. Gaponov, and N. Ducros, "All semiconductor enhanced high-harmonic generation from a single nanostructured cone," Sci. Rep. **9**, 5663 (2019).
[24]M. Sivis, M. Taucer, G. Vampa, K. Johnston, A. Staudte, A. Y. Naumov, D. M. Villeneuve, C. Ropers, and P. B. Corkum, "Tailored semiconductors for high-harmonic optoelectronics," Science **357**, 303–306 (2017).
[25]A. J. Uzan, G. Orenstein, Á. Jiménez-Galán, C. McDonald, R. E. F. Silva, B. D. Bruner, N. D. Klimkin, V. Blanchet, and T. Arusi-Parpar, "Attosecond spectral singularities in solid-state high-harmonic generation," Nat. Photonics **14**, 183–187 (2020).
[26]T. Higuchi, M. I. Stockman, and P. Hommelhoff, "Strong-field perspective on high-harmonic radiation from bulk solids," Phys. Rev. Lett. **113**, 213901 (2014).
[27]E. N. Osika, A. Chacón, L. Ortmann, N. Suárez, J. A. Pérez-Hernández, B. Szafran, M. F. Ciappina, F. Sols, A. S. Landsman, and M. Lewenstein, "Wannier-Bloch approach to localization in high-harmonics generation in solids," Phys. Rev. X **7**, 021017 (2017).
[28]M. Wu, D. A. Browne, K. J. Schafer, and M. B. Gaarde, "Multilevel perspective on high-order harmonic generation in solids," Phys. Rev. A **94**, 063403 (2016).
[29]A. M. Parks, G. Ernotte, A. Thorpe, C. R. McDonald, P. B. Corkum, M. Taucer, and T. Brabec, "Wannier quasi-classical approach to high harmonic generation in semiconductors," Optica **7**, 1764–1772 (2020).
[30]O. Schubert, M. Hohenleutner, F. Langer, B. Urbanek, C. Lange, U. Huttner, D. Golde, T. Meier, M. Kira, S. W. Koch, and R. Huber, "Sub-cycle control of terahertz high-harmonic generation by dynamical Bloch oscillations," Nat. Photonics **8**, 119–123 (2014).
[31]T. T. Luu, M. Garg, S. Y. Kruchinin, A. Moulet, M. T. Hassan, and E. Goulielmakis, "Extreme ultraviolet high-harmonic spectroscopy of solids," Nature **521**, 498–502 (2015).
[32]N. Tancogne-Dejean, O. D. Mücke, F. X. Kärtner, and A. Rubio, "Impact of the electronic band structure in high-harmonic generation spectra of solids," Phys. Rev. Lett. **118**, 087403 (2017).
[33]G. Vampa, C. R. McDonald, G. Orlando, D. D. Klug, P. B. Corkum, and T. Brabec, "Theoretical analysis of high-harmonic generation in solids," Phys. Rev. Lett. **113**, 073901 (2014).
[34]D. Golde, T. Meier, and S. W. Koch, "High harmonics generated in semiconductor nanostructures by the coupled dynamics of optical inter and intraband excitations," Phys. Rev. B **77**, 075330 (2008).
[35]G. Ndabashimiye, S. Ghimire, M. Wu, D. A. Browne, K. J. Schafer, M. B. Gaarde, and D. A. Reis, "Solid-state harmonics beyond the atomic limit," Nature **534**, 520–523 (2016).
[36]G. Vampa, C. R. McDonald, G. Orlando, P. B. Corkum, and T. Brabec, "Semiclassical analysis of high harmonic generation in bulk crystals," Phys. Rev. B **91**, 064302 (2015).
[37]L. Plaja and L. Roso-Franco, "High-order harmonic generation in a crystalline solid," Phys. Rev. B **45**, 8334–8341 (1992).
[38]M. Wu, S. Ghimire, D. A. Reis, K. J. Schafer, and M. B. Gaarde, "High-harmonic generation from Bloch electrons in solids," Phys. Rev. A **91**, 043839 (2015).
[39]E. Runge and E. K. U. Gross, "Density-functional theory for time-dependent systems," Phys. Rev. Lett. **52**, 997–1000 (1984).
[40]E. K. U. Gross and W. Kohn, "Time-dependent density-functional theory," Adv. Quantum Chem. **21**, 255–291 (1990).
[41]M. A. L. Marques and E. K. U. Gross, "Time-dependent density functional theory," Annu. Rev. Phys. Chem. **55**, 427–455 (2004).
[42]Z. Nourbakhsh, N. Tancogne-Dejean, H. Merdji, and A. Rubio, "High harmonics and isolated attosecond pulses from MgO," Phys. Rev. Appl. **15**, 014013 (2021).
[43]G. Wachter, C. Lemell, J. Burgdörfer, S. A. Sato, X. M. Tong, and K. Yabana, "Ab initio simulation of electrical currents induced by ultrafast laser excitation of dielectric materials," Phys. Rev. Lett. **113**, 087401 (2014).
[44]D. Bauer and K. K. Hansen, "High-harmonic generation in solids with and without topological edge states," Phys. Rev. Lett. **120**, 177401 (2018).

[45]N. Tancogne-Dejean, M. A. Sentef, and A. Rubio, "Ultrafast modification of Hubbard *U* in a strongly correlated material: *Ab initio* high-harmonic generation in NiO," Phys. Rev. Lett. **121**, 097402 (2018).
[46]I. Floss, C. Lemell, G. Wachter, V. Smejkal, S. A. Sato, X.-M. Tong, K. Yabana, and J. Burgdörfer, "*Ab initio* multiscale simulation of high-order harmonic generation in solids," Phys. Rev. A **97**, 011401 (2018).
[47]F. Dong, Q. Xia, and J. Liu, "Ellipticity of the harmonic emission from graphene irradiated by a linearly polarized laser," Phys. Rev. A **104**, 033119 (2021).
[48]M. Marques, A. Castro, G. F. Bertsch, and A. Rubio, "Octopus: A first-principles tool for excited electron–ion dynamics," Comput. Phys. Commun. **151**, 60–78 (2003).
[49]A. Castro, H. Appel, M. Oliveira, C. A. Rozzi, X. Andrade, F. Lorenzen, M. A. L. Marques, E. K. U. Gross, and A. Rubio, "*Octopus*: A tool for the application of time-dependent density functional theory," Phys. Status Solidi B **243**, 2465–2488 (2006).
[50]X. Andrade, D. Strubbe, U. De Giovannini, A. H. Larsen, M. J. T. Oliveira, J. Alberdi-Rodriguez, A. Varas, I. Theophilou, N. Helbig, M. J. Verstraete, L. Stella, F. Nogueira, A. Aspuru-Guzik, A. Castro, M. A. L. Marques, and A. Rubio, "Real-space grids and the octopus code as tools for the development of new simulation approaches for electronic systems," Phys. Chem. Chem. Phys. **17**, 31371–31396 (2015).
[51]N. Tancogne-Dejean, M. J. T. Oliveira, X. Andrade, H. Appel, C. H. Borca, G. Le Breton, F. Buchholz, A. Castro, S. Corni, A. A. Correa, U. De Giovannini, A. Delgado, F. G. Eich, J. Flick, and G. Gil, "Octopus, a computational framework for exploring light-driven phenomena and quantum dynamics in extended and finite systems," J. Chem. Phys. **152**, 124119 (2020).
[52]J. L. Krause, K. J. Schafer, and K. C. Kulander, "High-order harmonic generation from atoms and ions in the high intensity regime," Phys. Rev. Lett. **68**, 3535–3538 (1992).
[53]R. van Leeuwen, "Mapping from densities to potentials in time-dependent density-functional theory," Phys. Rev. Lett. **82**, 3863–3866 (1999).
[54]M. Greiner, O. Mandel, T. Esslinger, T. W. Hänsch, and I. Bloch, "Quantum phase transition from a superfluid to a Mott insulator in a gas of ultracold atoms," Nature **415**, 39–44 (2002).
[55]U. De Giovannini, A. H. Larsen, and A. Rubio, "Modeling electron dynamics coupled to continuum states in finite volumes with absorbing boundaries," Eur. Phys. J. B **88**, 56 (2015).
[56]H. J. Monkhorst and J. D. Pack, "Special points for Brillouin-zone integrations," Phys. Rev. B **13**, 5188–5192 (1976).
[57]J. P. Perdew and A. Zunger, "Self-interaction correction to density-functional approximations for many-electron systems," Phys. Rev. B **23**, 5048–5079 (1981).
[58]N. Troullier and J. L. Martins, "Efficient pseudopotentials for plane-wave calculations," Phys. Rev. B **43**, 1993–2006 (1991).
[59]P. Hohenberg and W. Kohn, "Inhomogeneous electron gas," Phys. Rev. **136**, B864–B871 (1964).
[60]W. Kohn and L. J. Sham, "Self-consistent equations including exchange and correlation effects," Phys. Rev. **140**, A1133–A1138 (1965).
[61]K. K. Hansen, D. Bauer, and L. B. Madsen, "Finite-system effects on high-order harmonic generation: From atoms to solids," Phys. Rev. A **97**, 043424 (2018).
[62]T. Meier, G. von Plessen, P. Thomas, and S. W. Koch, "Coherent electric-field effects in semiconductors," Phys. Rev. Lett. **73**, 902–905 (1994).